Analyzing the tidal-related origin of subinertial flows through the Strait of Gibraltar

M. Bruno,[1] J. Macías,[2] J. M. González-Vida,[3] and A. Vázquez[1]

[1]   The effects of tidal dynamics on subinertial flows through the Strait of Gibraltar are analyzed. As found in previous studies, an empirical orthogonal function analysis of subinertial currents at the Camarinal Sill yields two dominant oscillation modes. The first mode presents a barotropic character and rather irregular fluctuations and it has been related to meteorological forcing. The second mode is baroclinic and presents a clear deterministic behavior with time that seems to be related to tidal forcing. Against the hypothesis proposed in previous studies stating that tidal mixing cycles explain the second mode, we show, by using a one-dimensional numerical model of two-layer immiscible shallow water, that the origin of this mode may basically be related to nonlinear interactions among the main semidiurnal tidal constituents through the advective terms in the momentum balance and other nonlinear terms in the volume conservation equations. That mode is also crucial to understanding the vertical shear time variations of the horizontal currents. In particular, it minimizes the differences in the maximum shear between neap and spring tides.

Citation: Bruno, M., J. Macías, J. M. González-Vida, and A. Vázquez (2010), Analyzing the tidal-related origin of subinertial flows through the Strait of Gibraltar, *J. Geophys. Res.*, *115*, C12075, doi:10.1029/2010JC006499.

1.   Introduction

[2]   Flow variability through the Strait of Gibraltar can basically be categorized into three distinct types: long-term, subinertial and tidal [*Lacombe and Richez*, 1982]. The long-term flow exhibits a seasonal and interannual variability and relates to the two-layer baroclinic exchange, whereas subinertial flows, with periods ranging from days to a few months, are mostly barotropic and have been found to be mainly forced by the fluctuations in atmospheric pressure over the Mediterranean Sea. However, a significant part of the variance of subinertial fluctuations has been related to tidal forcing.

[3]   Using empirical orthogonal function (EOF) analysis of subinertial velocity time series recorded over the Camarinal Sill, *Candela et al.* [1989] isolated two dominant oscillation modes. The first mode (explaining about 80% of variance) was related to the fluctuations in atmospheric pressure over the western Mediterranean, and presented an almost barotropic character. The second mode (explaining about 15% of variance) was related to tidal forcing, and presented a baroclinic behavior and very regular fortnightly and monthly periodicities.

[4]   Although the tidal origin of this second mode seems widely accepted, the actual mechanism by which it arises remains unclear. The baroclinic character of the second mode, with opposite current directions above and below the pycnocline, was responsible for the observed temporal variations of the vertical shear that reaches maximum/minimum values during neap/spring tides [*Candela et al.*, 1989]. Taking this fact into account, *Bryden et al.* [1994] and *Vargas et al.* [2006] stated that variation in tidal mixing intensity between spring and neap tides cycles may be a very likely mechanism. Thus the two-layer flow exchange through the Strait of Gibraltar is maximized during neap tides due to a greater contrast in density between the basins associated with reduced mixing, and minimized during spring tides when there is less difference in density due to more intensive mixing. On the other hand, although not explicitly, the results reported in other works [*Farmer and Armi*, 1986; *Helfrich*, 1995; *Brandt et al.*, 2004] indicate that the time-dependent hydraulic control over Camarinal Sill forced by barotropic tidal flows could contribute to the creation of certain subinertial variability.

[5]   In this article, we show that nonlinear interactions among the signals of the three main semidiurnal constituents, M_2, S_2 and N_2, may be able to generate the baroclinic fortnightly and monthly signals appearing in the second EOF mode of subinertial fluctuations.

[6]   The article is organized as follows: Section 2 describes the analysis of the current velocity observations. Results from the numerical experiments with a two-layer, shallow water numerical model are described in section 3. In section 4, an analytical explanation for the nonlinear

---
[1]Departamento de Física Aplicada, Universidad de Cádiz, Cadiz, Spain.
[2]Departamento de Análisis Matemático, Universidad de Málaga, Malaga, Spain.
[3]Departamento de Matemática Aplicada, Universidad de Málaga, Malaga, Spain.
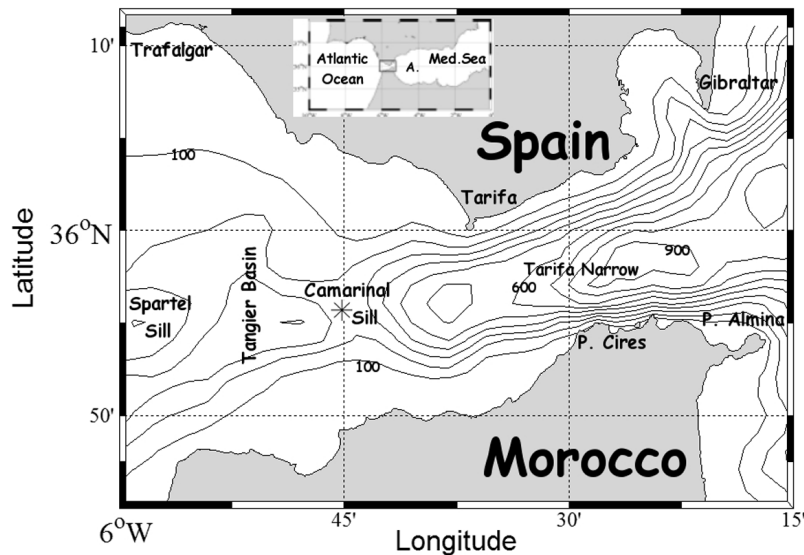
Figure 1. Map of the Strait of Gibraltar. The star indicates the site where used ADCP data were collected. Numbers indicate the corresponding bottom depth of the isobaths.

origin of fortnightly and monthly signals in the flow variables is given. In section 5 there is a general discussion of the results, and finally some conclusions are drawn.

2. Current Velocity Observations

[7] The time series for the current velocity used in this work have been extracted from recorded profiles taken by a 150 KHz ADCP, moored directly over the Camarinal Sill (see map in Figure 1), in a water column of about 280 m depth. The sampling interval was 15 min and the vertical resolution was 10 m spanning from 45 to 265 m depth. Those data were collected during the experiment "Strait 94-96," from October 1994 to October 1996. In the present analysis we will focus on a 6 month long segment of measurements (from October 1995 to March 1996) during which a continuous record (without any gaps) of current velocity was obtained.

[8] From these records the deterministic part of the subinertial signal will be estimated. The analysis will refer to the west-east component of current velocity that coincides fairly well with the predominant direction in the region of the Camarinal Sill.

[9] As the first step in the analysis, the subinertial signal must be isolated from the original records. To do this, a low-pass filter for removing signals with periods smaller than 33 h was applied to the original time series. Then, as *Candela et al.* [1989] and *Vargas et al.* [2006] did, an EOF analysis was applied to subinertial series at all depths in order to isolate the deterministic part of the signal. This practice is necessary to prevent meteorological variability from contaminating the subsequent harmonic analysis, since a substantial proportion of total variance of the meteorological fluctuations is located around the fortnightly and monthly frequencies.

[10] The results from this analysis are illustrated in Figures 2 and 3 where it can be seen that only two modes explain more than 95% of the subinertial current variance

throughout the water column over the Camarinal Sill. As expected, the temporal weights of the first mode exhibit a rather irregular fluctutations and a barotropic character (positive spatial weights at all depths), while the second mode shows a clear periodic behavior in time and a clear
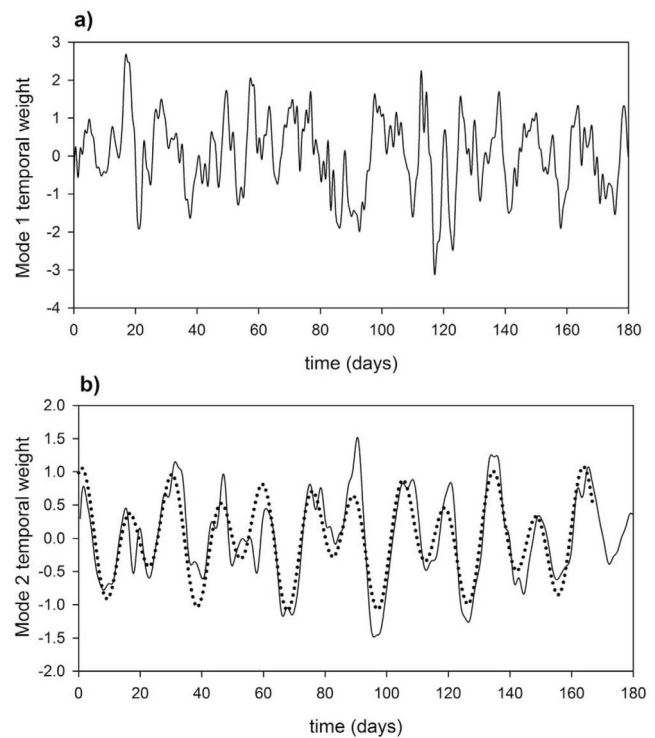

Figure 2. Temporal weights for the two first EOF modes of subinertial currents at Camarinal Sill: (a) mode 1 and (b) mode 2. In Figure 2b the dotted curve is the prediction using *Msf* and *Mm* harmonics resolved from the least squares analysis on mode 2 temporal weights.
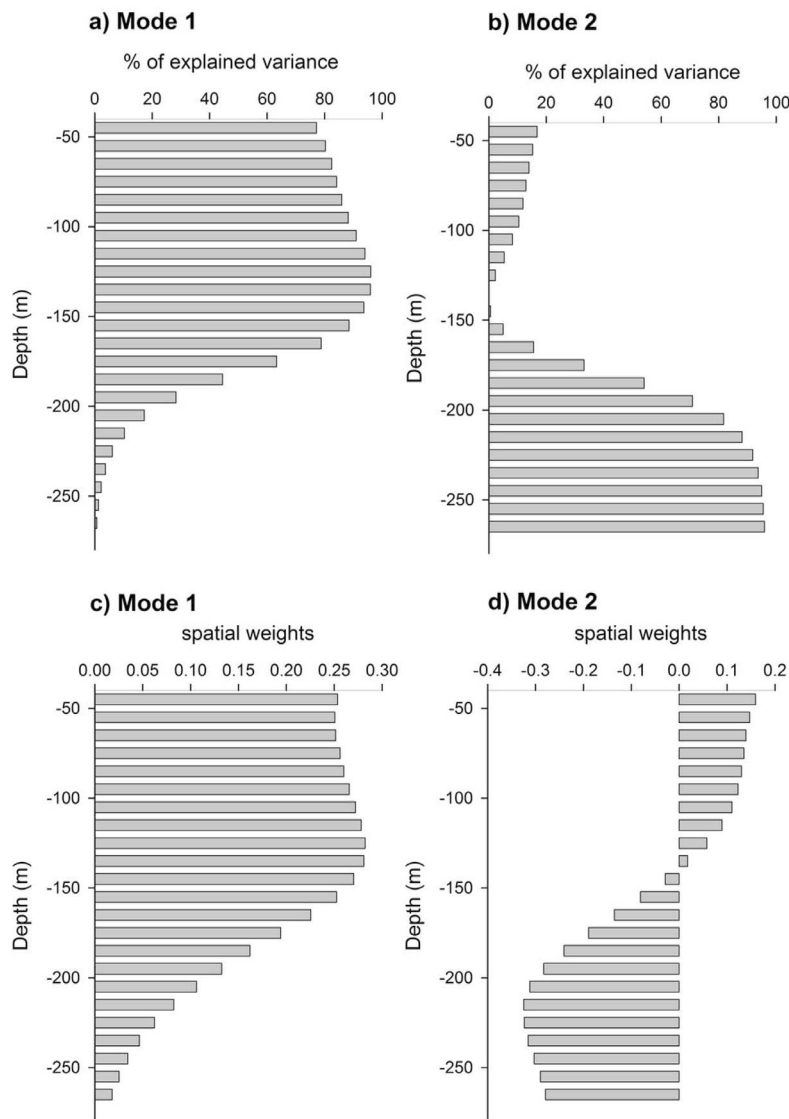
Figure 3. The percentages of variance explained for the two first EOF modes are shown: (a) mode 1 and (b) mode 2. The corresponding spatial weights (c) mode 1 and (d) mode 2 are also shown.

baroclinic character (spatial weights change their sign at a given depth). It should be noted in Figure 3b that, while the deterministic mode explains only about 15% of the subinertial variance in the upper layer (0–130 m), in the lower layer (130–300 m) it is the dominant mode, and at this depth it explains about 70% of the total variance. Layer thickness were determined using the mean interface depth, assuming that this depth is located where the vertical profile of mean current changes from positive (toward east) to negative (toward west) [*Tsimplis and Bryden*, 2000].

[11] This second mode will serve as a basis for determining the harmonic constants for Msf and Mm constituents in the subinertial currents at the Camarinal Sill. To do that, a least squares harmonic analysis [*Foreman and Henri*, 1989] is applied to the temporal weights of the second mode. In Figure 2b it can be seen that the harmonic prediction made using the computed harmonic constants for Msf and Mm signals presents a fairly good fit to the behavior of mode 2

temporal weights, confirming the deterministic nature of this mode.

[12] To compute amplitudes and Greenwich phases of current velocity throughout the water column, the harmonic constants of mode 2 temporal weights are computed using the corresponding spatial weights (see Figure 2b) at each depth. Finally these harmonic constants are vertically averaged within the upper and lower layers. The resulting values for the two layers are shown in Table 1.

3. Numerical Experiments

[13] The objective of the numerical model experiments is to investigate whether realistic fortnightly and monthly signals of subinertial flows can be explained in the framework equations of motion of nonmiscible fluids. A numerical model that considers 1-D, two-layer, shallow water equations for channels with irregular geometry, in both

Table 1. Amplitudes and Greenwich Phases Values for Msf and Mm Harmonics at Camarinal Sill as Calculated From Observations and Numerical Model[a]

	Observations		Numerical Model	
Harmonic	U (m/s)	g (deg)	U (m/s)	g (deg)
Msf	0.075 (0.16)	193.45 (27.86)	0.08 (0.15)	200.00 (27.38)
Mm	0.045 (0.10)	207.86 (13.45)	0.04 (0.07)	198.21 (15.91)

[a]Here U is the amplitude and g is the Greenwich phase. Values outside (inside) parentheses correspond to upper (lower) layer.

width and depth, will be used. This general formulation extends the one-layer shallow water equations and takes into account all the sources and coupling terms due to the difference in density between layers, as well as the terms due to the geometry. Models of this kind have been used widely in oceanographic applications, but mainly for channels with rectangular, or sometimes triangular, cross section. In this work, the model takes into account more general cross sections, symmetric but arbitrary in shape; this introduces a more complex shallow water equation system, and makes the numerical solution of the equations much more difficult since the counterpart to the effects of the complex geometry of the Strait of Gibraltar are included in the one-dimensional model.

[14] The working hypothesis adopted in conducting the experiments is that those signals may be generated through the nonlinear terms contained in the momentum balance and volume conservation. The advective acceleration and friction at bottom, the lateral boundaries and the interface separating the two layers will be considered within the momentum balance. By comparing experiments with and without friction terms, the relative importance of those terms in generating the investigated subinertial signals can be assessed.

3.1. Model Equations

[15] The numerical model used is well described by *Castro et al.* [2001, 2004a, 2004b]. All we will do here is briefly introduce the model equations and direct the reader to the cited references for further details. Some notation needs to be introduced first. In general, subscripts 1 and 2 mean "for upper and lower layers," respectively. The coordinate x refers to the axis of the channel; y is the horizontal coordinate normal to the axis; z is the vertical spatial coordinate; t is the time; g is the gravity; ρ_i is the density of the ith layer ($\rho_1 < \rho_2$), $r = \rho_1/\rho_2$. Variables $b(x)$ and $\sigma(x,z)$ are bottom and width functions, respectively, i.e., channel bottom is defined by the surface of equation: $z = b(x)$, and channel walls by the equations: $y = \pm(1/2)\sigma(x,z)$. The variables $A_i(x,t)$ and $h_i(x,t)$ represent the wetted cross section and the thickness of the ith layer at the section of coordinate at time t (see Figure 4), respectively. Therefore A_i and h_i ($i = 1,2$) are related through the equations

$$A_1 = \int_{b(x)+h_2}^{b(x)+h_1+h_2} \sigma(x,z)dz$$

$$A_2 = \int_{b(x)}^{b(x)+h_2} \sigma(x,z)dz.$$

Finally, $v_i(x,t)$ and $Q_i(x,t) = v_i(x,t)A_i(x,t)$ represent the velocity and the transport of the ith layer.

[16] The general equations governing the one-dimensional flow of two shallow layers of immiscible fluids (volume conservation and momentum balance) along a straight channel with symmetric cross section of arbitrary shape can be written as follows:

Upper layer

$$\frac{\partial A_1}{\partial t} + \frac{\partial Q_1}{\partial x} = 0$$

$$\frac{\partial Q_1}{\partial t} + \frac{\partial}{\partial x}\left(\frac{Q_1^2}{A_1} + \frac{g}{2\sigma_1}A_1^2\right) = -g\frac{A_1}{\sigma_1}\frac{\partial A_2}{\partial x} + \frac{g}{2}\left(\frac{1}{\sigma_1}\right)_x A_1^2 + g\frac{A_1}{\sigma_1}$$
$$\cdot \int_b^{b+h_1+h_2} \frac{\partial\sigma}{\partial x}dz$$
$$- gA_1\frac{\sigma_b}{\sigma_1}\frac{db}{dx} + F_1 \qquad (1)$$

Lower layer

$$\frac{\partial A_2}{\partial t} + \frac{\partial Q_2}{\partial x} = 0$$

$$\frac{\partial Q_2}{\partial t} + \frac{\partial}{\partial x}\left(\frac{Q_2^2}{A_2} + \frac{g}{2\sigma_2}A_2^2\right) = -gr\frac{A_2}{\sigma_1}\frac{\partial A_1}{\partial x} + \frac{g}{2}\left(\frac{1}{\sigma_2}\right)_x A_2^2$$
$$+ g\left(\frac{r}{\sigma_1}\int_b^{b+h_1+h_2}\frac{\partial\sigma}{\partial x}dz + \frac{1-r}{\sigma_3}\int_b^{b+h_2}\frac{\partial\sigma}{\partial x}dz\right)$$
$$- gA_2\frac{\sigma_b}{\sigma_2}\frac{db}{dx} + F_2, \qquad (2)$$

where $\sigma_1(x,t) = \sigma[x,b(x) + h_2(x,t) + h_1(x,t)]$ is the channel width at the free surface; $\sigma_3(x,t) = \sigma[x,b(x) + h_2(x,t)]$ is the channel width at the interface; $\sigma_b(x,t) = \sigma[x,b(x)]$ is the channel width at the bottom. Functions σ_1, σ_2 and σ_3 are related through the expression $\frac{1}{\sigma_2} = \frac{1-r}{\sigma_3} - \frac{r}{\sigma_1}$. Finally the terms F_1 and F_2 are parameterized friction effects on each layer and read as

$$F_1 = \frac{1}{\rho_1}\left[-\tau_{b,1}(\sigma_1 - \sigma_3)\right] \qquad (3)$$

$$F_2 = \frac{\sigma_3}{\rho_2}\left(\tau_{\text{int}} - \tau_{b,2}\right), \qquad (4)$$

where $\tau_{\text{int}} = \rho_1 r_{\text{int}}(u_1 - u_2)|u_1 - u_2|$, $\tau_{b,1} = \rho_1 r_b u_1|u_1|$ and $\tau_{b,2} = \rho_1 r_b u_2|u_2|$. τ_{int} is the friction stress at the interface between layers, while $\tau_{b,1}$ and $\tau_{b,2}$ are the friction stresses on the lateral boundaries or bottom; u_i ($i = 1,2$) are the velocities of the upper ($i = 1$) and lower ($i = 2$) layers; r_{int} and $r_{b,i}$ ($i = 1,2$) are interfacial and bottom friction coefficients. Note that friction at the sea surface is not considered.

[17] The model approximates the actual geometry of the Strait by using appropriate width and bottom functions. To determine those functions, we use bathymetric data to construct an equivalent symmetric channel with identical areas as actual transverse sections. After defining an along-strait axis, we consider $M = 200$ transverse sections along it at intervals $\Delta x \sim 600$ m, whose areas S_i, $i = 1,..., M$, are numerically computed. The bottom depth assigned to each section is taken as the maximum value, h_i, found in the bathymetric data. Finally, the channel width of the sections
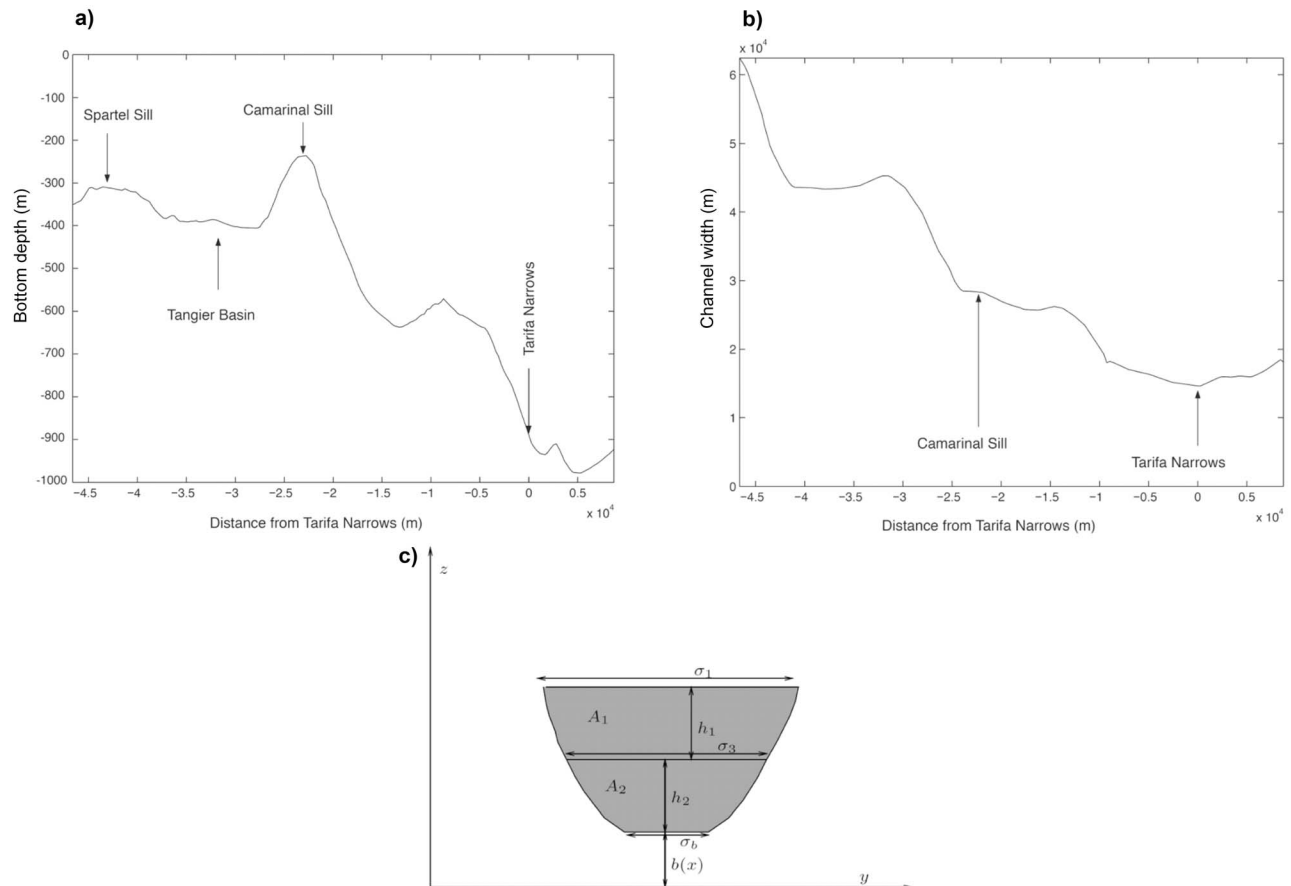
Figure 4. Information about the channel geometry used to adapt the actual geometry of the Strait of Gibraltar: (a) bottom topography, (b) channel width at sea surface along longitudinal axis, and (c) notation for channel cross sections.

is approximated by a continuous piecewise linear function constructed in such a way that cross-sectional areas for the model are the same as actual values. Figures 4a and 4b show the bottom function and the width at the top of the channel obtained from this procedure.

3.2. Model Results

[18] Tidal simulation experiments are performed by imposing on the steady state solution, resulting from a "lock exchange" problem, a tidal forcing at the open boundaries of the channel prescribed in terms of harmonic constants of the main tidal constituents of the surface tide: M_2, S_2, N_2, K_1 and O_1. Boundary conditions are obtained from *García la Fuente et al.* [1990].

[19] We have performed two experiments: one disregarding the friction terms, and the another considering a friction term parameterized as in equations (3) and (4), using the values $r_{int} = 10^{-4}$, $r_{b,1} = r_{b,2} = 10^{-3}$, $\rho_1 = 1027$ Kg m^{-3} and $\rho_2 = 1029$ Kg m^{-3} which lie within the range of values used by other authors [*Izquierdo et al.*, 2001].

[20] Figure 5 shows the comparison, for the cross section of the Camarinal Sill, between subinertial current velocities simulated by the model and the deterministic fluctuations of subinertial currents constructed using the temporal and spatial weights of the deterministic mode found in the EOF analysis of subinertial current records. Simulated subinertial currents

were obtained by applying a low-pass filter on variables of the initial output, to remove signals with periods shorter than 33 h. Table 1 shows a comparison of the harmonic constants of Msf and Mm signals corresponding to the model and the observations. As can be seen, the simulated series are in very good agreement with those extracted from the observations. This result seems to demonstrate that the deterministic mode of the subinertial currents over the Camarinal Sill may be explained using a nonmiscible and nonlinear model without the involvement of mixing phenomena.

[21] From inspection of Figure 5, it is also inferred that friction is not the dominant nonlinear mechanism for explaining the subinertial signals originated; therefore they must be explained through the other nonlinear terms, i.e., advective terms in the momentum balance, and nonlinear terms in the volume conservation equation.

4. An Analytical Explanation for Subinertial Tidal Flows

[22] As commented in the Introduction, fortnightly and monthly signals in the Strait of Gibraltar have previously been related to variations in the tidal mixing intensity during the spring-neap tidal cycle. In contrast, in section 3.2, we have shown, by the use of a nonlinear numerical model, that such signals may be generated without invoking mixing
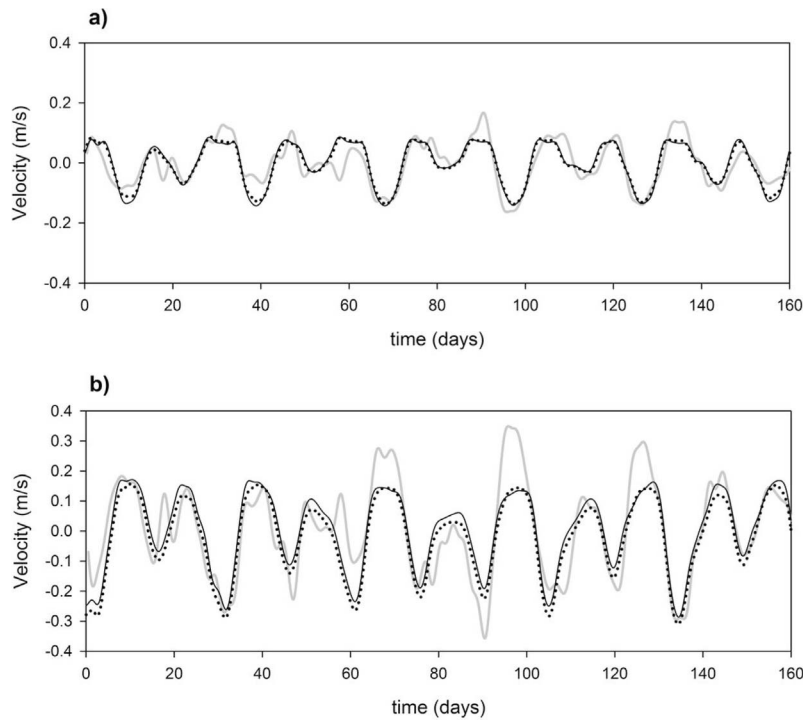
Figure 5. Time series of current velocity at Camarinal Sill cross section. Simulated by the numerical model without (black curve) and with (dotted curve) friction and deterministic subinertial currents constructed using the EOF analysis results (gray curve): (a) upper layer and (b) lower layer. Series begin at 0000 UTC on 16 October 16 1995.

phenomena. Furthermore, nonlinear effects due to friction at the interface and bottom do not seem to contribute significantly to creating these signals. In the following paragraphs we will present a suitable physical interpretation of the phenomenon, in the framework of the nonlinear equations of motion for the immiscible and frictionless 1-D, two-layer problem in a channel of rectangular and constant transverse section

$$-\frac{\partial \xi_i}{\partial t} + \frac{\partial}{\partial x}[u_1(d_1 - \xi_i)] = 0 \tag{5}$$

$$\frac{\partial \xi_i}{\partial t} + \frac{\partial}{\partial x}[u_2(d_2 + \xi_i)] = 0 \tag{6}$$

for volume conservation and

$$\frac{\partial u_1}{\partial t} + u_1 \frac{\partial u_1}{\partial x} = -g\frac{\partial \xi_s}{\partial x} \tag{7}$$

$$\frac{\partial u_2}{\partial t} + u_2 \frac{\partial u_2}{\partial x} = -g'\frac{\partial \xi_i}{\partial x} + g\frac{\rho_1}{\rho_2} \frac{\partial \xi_s}{\partial x} \tag{8}$$

for momentum balance. Again, subscripts 1 and 2 stand for upper and lower layers respectively; d_1 and d_2 are the long-term time-averaged thickness of the layers; ξ_s and ξ_i are vertical displacement from their mean positions of sea surface level and the interface separating the two layers, respectively; u_1 and u_2 are the velocities in upper and lower layers; g' is reduced gravity $g' = g(\rho_2 - \rho_1)/\rho_2$; t and x are the

time and space coordinates. Notice that the "rigid lid" assumption at the sea surface has been applied in volume conservation equations.

[23] The variables u_1, u_2, ξ_s and ξ_i can be expanded in terms of the small parameter $\varepsilon = A/D$, with A and D standing for characteristic values for amplitude of vertical displacement of interface and total depth of the water column in the region of interest, as follows:

$$u_1 = u_1^0 + \varepsilon u_1^1, \tag{9}$$

$$u_2 = u_2^0 + \varepsilon u_2^1, \tag{10}$$

$$\xi_i = \xi_i^0 + \varepsilon \xi_i^1, \tag{11}$$

$$\xi_s = \xi_s^0 + \varepsilon \xi_s^1. \tag{12}$$

Substitution of those expansions in equations (5)–(8), after disregarding terms with powers of ε greater than one, yields the following zero- and first-order balances:
Zero-order volume conservation

$$-\frac{\partial \xi_i^0}{\partial t} + d_1 \frac{\partial u_1^0}{\partial x} = 0, \tag{13}$$

$$\frac{\partial \xi_i^0}{\partial t} + d_2 \frac{\partial u_2^0}{\partial x} = 0, \tag{14}$$

Zero-order momentum balance

$$\frac{\partial u_1^0}{\partial t} = -g\frac{\partial \xi_s^0}{\partial x}, \tag{15}$$

$$\frac{\partial u_1^0}{\partial t} = -g'\frac{\partial \xi_i^0}{\partial x} - g\frac{\rho_1}{\rho_2}\frac{\partial \xi_s^0}{\partial x}, \tag{16}$$

First-order volume conservation

$$\varepsilon\left[-\frac{\partial \xi_i^1}{\partial t} + d_1\frac{\partial u_1^1}{\partial x} - \frac{\partial}{\partial x}\left(u_1^0\xi_i^1 + \xi_i^0 u_1^1\right)\right] = \frac{\partial}{\partial x}\left(u_1^0\xi_i^0\right), \tag{17}$$

$$\varepsilon\left[\frac{\partial \xi_i^1}{\partial t} + d_2\frac{\partial u_2^1}{\partial x} + \frac{\partial}{\partial x}\left(u_2^0\xi_i^1 + \xi_i^0 u_2^1\right)\right] = -\frac{\partial}{\partial x}\left(u_2^0\xi_i^0\right), \tag{18}$$

First-order momentum balance

$$\varepsilon\left[\frac{\partial u_1^1}{\partial t} + \frac{\partial}{\partial x}\left(u_1^0 u_1^1\right) + g\frac{\partial \xi_s^1}{\partial x}\right] = -\frac{1}{2}\frac{\partial}{\partial x}\left[\left(u_1^0\right)^2\right], \tag{19}$$

$$\varepsilon\left[\frac{\partial u_2^1}{\partial t} + \frac{\partial}{\partial x}\left(u_2^0 u_2^1\right) + g'\frac{\partial \xi_i^1}{\partial x} + g\frac{\rho_1}{\rho_2}\frac{\partial \xi_s^1}{\partial x}\right] = -\frac{1}{2}\frac{\partial}{\partial x}\left[\left(u_2^0\right)^2\right]. \tag{20}$$

[24] In order to characterize the spectral composition of the first-order variables, the zero-order variables can be expressed as the sum of a mean value plus the contribution of several tidal constituents

$$u_k^0 = \bar{u}_k + \sum_{m=1}^{M} U_k^m \cos\left(\omega_m t - g_{u_k}^m\right), \tag{21}$$

$$\xi_i^0 = \bar{\xi}_i + \sum_{m=1}^{M} A_i^m \cos\left(\omega_m t - g_i^m\right), \tag{22}$$

$$\xi_s^0 = \bar{\xi}_s + \sum_{m=1}^{M} A_s^m \cos\left(\omega_m t - g_s^m\right), \tag{23}$$

where $k = 1,2$ refers to upper or lower layer; M is the number of tidal constituents; the overbars stand for long-term time-averaged values of the variables; U_{is} and A_{is} are amplitudes of the tidal constituent signals in the velocity, sea level and interface displacements; ω_{is} stand for angular frequency of tidal constituents; g_{is} are the Greenwich phase lag of each tidal constituent for the different variables.

[25] It can be deduced from the first-order equations that frequencies of first-order variables are defined by those periods arising from the terms on the right-hand side of equations (17)–(20). After substituting the expressions (21)–(23) in the right-hand side of equations (17)–(20), the terms appearing derived with x give the following:

$$u_k^0\xi_i^0 = \bar{\xi}_i\left[\bar{u}_k + \sum_{m=1}^{2} U_k^m \cos\left(\omega_m t - g_{u_k}^m\right)\right]$$
$$+ \bar{u}_k + \sum_{m=1}^{2} A_i^m \cos\left(\omega_m t - g_i^m\right) + \sum_{m=1}^{2}\sum_{n=1}^{2} A_i^n U_k^m$$
$$\cdot \cos\left(\omega_n t - g_i^n\right)\cos\left(\omega_m t - g_{u_k}^m\right) \tag{24}$$

$$\left(u_k^0\right)^2 = \bar{u}_k\left[\bar{u}_k + 2\sum_{m=1}^{2} U_k^m \cos\left(\omega_m t - g_{u_k}^m\right)\right]$$
$$+ \sum_{m=1}^{2}\sum_{n=1}^{2} U_k^n U_k^m \cos\left(\omega_n t - g_{u_k}^n\right)\cos\left(\omega_m t - g_{u_k}^m\right). \tag{25}$$

Note on the right-hand side of those expression that the contribution of the first and second terms in (24), and the first term in (25), is located at the basic tidal frequencies and mean value, so they are not of interest in our problem. However, the last terms of the two expressions create higher and lower frequencies lying outside the basic tidal bands. Those terms may be rewritten as

$$\sum_{m=1}^{2}\sum_{n=1}^{2} A_i^n U_k^m \cos\left(\omega_n t - g_i^n\right)\cos\left(\omega_m t - g_{u_k}^m\right)$$
$$= \frac{1}{2}\sum_{m=1}^{2}\sum_{n=1}^{2} A_i^n U_k^m \left\{\begin{array}{l}\cos\left[(\omega_n + \omega_m)t - \left(g_i^n + g_{u_k}^m\right)\right]\\ + \cos\left[(\omega_n - \omega_m)t - \left(g_i^n - g_{u_k}^m\right)\right]\end{array}\right\} \tag{26}$$

$$\sum_{m=1}^{2}\sum_{n=1}^{2} U_k^n U_k^m \cos\left(\omega_n t - g_{u_k}^n\right)\cos\left(\omega_m t - g_{u_k}^m\right)$$
$$= \frac{1}{2}\sum_{m=1}^{2}\sum_{n=1}^{2} U_k^n U_k^m \left\{\begin{array}{l}\cos\left[(\omega_n + \omega_m)t - \left(g_{u_k}^n + g_{u_k}^m\right)\right]\\ + \cos\left[(\omega_n - \omega_m)t - \left(g_{u_k}^n - g_{u_k}^m\right)\right]\end{array}\right\}, \tag{27}$$

where a given pair of n and m values correspond to a given pair of harmonic constituents. For $n = m$, second terms within the brackets {} give rise to a contribution to the mean value, while the first terms give rise to overharmonics like M_4, S_4 and N_4. For $n \neq m$, the second terms between the brackets give rise to overharmonics like MS_4, MN_4, SN_4 and lower frequency harmonics like the fortnightly (Msf) and monthly (Mm) which are of interest in this context. For instance, when n and m represent the pair of constituents M_2 and S_2, the double summation of (27) contains a Msf signal

$$U_k^{M_2} U_k^{S_2} \cos\left[\omega_{Msf} t - \left(g_{u_k}^{S_2} - g_{u_k}^{M_2}\right)\right]$$

and similarly, when the M_2 and N_2 pair is considered, there is a Mm signal

$$U_k^{M_2} U_k^{N_2} \cos\left[\omega_{Mm} t - \left(g_{u_k}^{M_2} - g_{u_k}^{N_2}\right)\right],$$

where $\omega_{Msf} = \omega_{S2} - \omega_{M2}$ and $\omega_{Mm} = \omega_{M2} - \omega_{N2}$. Therefore, the part of the terms on the right-hand side of equations (13)–(16) only containing the Msf and Mm signals may be written as

$$\langle u_1^0\xi_i^0\rangle = \frac{U_1^{M_2} A_i^{S_2}}{2}\cos\left[\omega_{Msf} t - \left(g_i^{S_2} - g_{u_1}^{M_2}\right)\right]$$
$$+ \frac{U_1^{S_2} A_i^{M_2}}{2}\cos\left[\omega_{Msf} t - \left(g_{u_1}^{S_2} - g_i^{M_2}\right)\right]$$
$$+ \frac{U_1^{M_2} A_i^{N_2}}{2}\cos\left[\omega_{Mm} t - \left(g_{u_1}^{M_2} - g_i^{N_2}\right)\right]$$
$$+ \frac{U_1^{N_2} A_i^{M_2}}{2}\cos\left[\omega_{Mm} t - \left(g_i^{M_2} - g_{u_1}^{N_2}\right)\right], \tag{28}$$

$$\langle u_2^0\xi_i^0\rangle = \frac{U_2^{M_2} A_i^{S_2}}{2}\cos\left[\omega_{Msf} t - \left(g_i^{S_2} - g_{u_2}^{M_2}\right)\right]$$
$$+ \frac{U_2^{S_2} A_i^{M_2}}{2}\cos\left[\omega_{Msf} t - \left(g_{u_2}^{S_2} - g_i^{M_2}\right)\right]$$
$$+ \frac{U_2^{M_2} A_i^{N_2}}{2}\cos\left[\omega_{Mm} t - \left(g_{u_2}^{M_2} - g_i^{N_2}\right)\right]$$
$$+ \frac{U_2^{N_2} A_i^{M_2}}{2}\cos\left[\omega_{Mm} t - \left(g_i^{M_2} - g_{u_2}^{N_2}\right)\right], \tag{29}$$

$$\left\langle (u_1^0)^2 \right\rangle = U_1^{M_2} U_1^{S_2} \cos\left[\omega_{Msf} t - \left(g_{u_1}^{S_2} - g_{u_1}^{M_2} \right) \right]$$
$$+ U_1^{M_2} U_1^{N_2} \cos\left[\omega_{Mm} t - \left(g_{u_1}^{M_2} - g_{u_1}^{N_2} \right) \right], \tag{30}$$

$$\left\langle (u_2^0)^2 \right\rangle = U_2^{M_2} U_2^{S_2} \cos\left[\omega_{Msf} t - \left(g_{u_2}^{S_2} - g_{u_2}^{M_2} \right) \right]$$
$$+ U_2^{M_2} U_2^{N_2} \cos\left[\omega_{Mm} t - \left(g_{u_2}^{M_2} - g_{u_2}^{N_2} \right) \right]. \tag{31}$$

[26] Hereinafter we will focus on the part of the first-order variables on the left-hand side of equations (17)–(20) that matches those low-frequency signals appearing in (28)–(31). Assuming that the first terms on the left-hand side of equations (17)–(20) vary only very slowly over time, their contributions can be disregarded. It should also be noted that the terms in the left-hand side of equations (17)–(20)

$$u_1^0 \xi_i^1, \ \xi_i^0 u_1^1, \ \xi_i^0 u_2^1, \ u_2^0 \xi_i^1, \ u_1^0 u_1^1, \ u_2^0 u_2^1,$$

consisting of products between zero- and first-order variables, would only match the spectral composition of the right-hand side terms for the mean value of zero-order variables. Finally, taking into account that the mean value of the variable is zero, first-order balances may be simplified to

$$\varepsilon \left[d_1 u_1^1 - \bar{u}_1 \xi_i^1 \right] = \left\langle u_1^0 \xi_i^0 \right\rangle, \tag{32}$$

$$\varepsilon \left[d_2 u_2^1 - \bar{u}_2 \xi_i^1 \right] = -\left\langle u_2^0 \xi_i^0 \right\rangle, \tag{33}$$

$$\varepsilon \left[\bar{u}_1 u_1^1 + g \xi_s^1 \right] = -\frac{\left\langle (u_1^0)^2 \right\rangle}{2}, \tag{34}$$

$$\varepsilon \left[\bar{u}_2 u_2^1 + g' \xi_i^1 + g \frac{\rho_1}{\rho_2} \xi_s^1 \right] = -\frac{\left\langle (u_2^0)^2 \right\rangle}{2}, \tag{35}$$

and solutions for first-order contribution may be then expressed as

$$\varepsilon \xi_i^1 = \frac{-\frac{\rho_1}{\rho_2} T_1 + T_2}{C}, \tag{36}$$

$$\varepsilon \xi_s^1 = \frac{\left[\frac{(\bar{u}_2)^2}{d_2} + g' \right] T_1 - \frac{(\bar{u}_1)^2}{d_1} T_2}{gC}, \tag{37}$$

$$\varepsilon u_1^1 = \frac{\left\langle u_1^0 \xi_i^0 \right\rangle}{d_1} - \frac{\bar{u}_1 \rho_1 T_1}{d_1 \rho_2 C} + \frac{\bar{u}_1 T_2}{d_1 C}, \tag{38}$$

$$\varepsilon u_2^1 = -\frac{\left\langle u_2^0 \xi_i^0 \right\rangle}{d_2} - \frac{\bar{u}_2 \rho_1 T_1}{d_2 \rho_2 C} + \frac{\bar{u}_2 T_2}{d_2 C}, \tag{39}$$

where

$$C = \left[\frac{(\bar{u}_2)^2}{d_2} + g' - \frac{\rho_1}{\rho_2} \frac{(\bar{u}_1)^2}{d_1} \right], \tag{40}$$

$$T_1 = -\frac{\bar{u}_1}{d_1} \left\langle u_1^0 \xi_i^0 \right\rangle - \frac{\left\langle (u_1^0)^2 \right\rangle}{2}, \tag{41}$$

$$T_2 = -\frac{\bar{u}_2}{d_2} \left\langle u_2^0 \xi_i^0 \right\rangle - \frac{\left\langle (u_2^0)^2 \right\rangle}{2}. \tag{42}$$

Table 2. Harmonic Constants for the Main Semidiurnal Tidal Constituents of Vertical Displacement of Interface and Current Velocity Simulated by the Numerical Model at the Place of the Mooring[a]

Harmonic	Model Current Velocity		Model Interface	
	U (m/s)	g_u (deg)	A (m)	g (deg)
N_2	0.22 (0.18)	137.00 (135.00)	8.00	349.00
M_2	1.09 (0.95)	149.00 (147.00)	40.00	3.20
S_2	0.42 (0.30)	180.00 (174.00)	16.00	32.44

[a]See map on Figure 1. Here U and g_u are the amplitude and Greenwich phase of tidal constituents for current velocity, A and g are the amplitude and Greenwich phase of tidal constituents for the interface displacement. Values outside (inside) parentheses correspond to upper (lower) layer current velocity.

[27] In order to evaluate the first-order analytical solution, it is necessary to prescribe values for the parameters appearing on the right-hand side of expressions (38) and (39). We obtain those values from the numerical model simulations on the cross section corresponding to the Camarinal Sill, described in section 3.2. Values for amplitudes and Greenwich phases of semidiurnal constituents for currents and vertical displacement of the interface are shown in Table 2. Values for mean currents in the upper and lower layers, $\bar{u}_1 = 0.31$ m/s and $\bar{u}_2 = -0.70$ m/s, are also taken from the numerical model simulations. Finally, the mean layer thickness values, $d_1 = 154$ m and $d_2 = 85$ m, are chosen in order to allow the quotient d_1/d_2 to keep the same proportion as the quotient between the time-averaged cross-channel upper and lower layer areas computed by the numerical model.

[28] The resulting temporal evolutions of first-order contribution given by equations (38) and (39) are shown in Figure 6 together with the subinertial currents simulated by the numerical model. As can be seen, the time series predicted by the analytical solution follow fairly well the basic behavior of that simulated by the numerical model time series. Discrepancies could be attributed to the fact that the numerical model accounts for additional nonlinear effects related to: (1) changes in the geometry of the cross section and (2) neglecting the time derivate of the first-order vertical displacement in equations (17) and (18), and (3) the time-dependent hydraulic control over the sill, which have not been accounted for in the analytical solution. Note that although these effects are not negligible, they seem to be of secondary importance.

5. Discussion

[29] It is should be noted that, in Figure 6, the contribution to the first-order solution from the sum of the two last terms on the right-hand side of equations (38) and (39) are very small in comparison with the first term. This fact may be explained if one considers that, since T_1 and T_2 are of similar size (see equations (41) and (42)), the second and third terms on the right-hand side of equations (38) and (39), which have different sign, tend to cancel each other out; the effect of this is to favor the dominance of the first term on the right-hand side in defining the
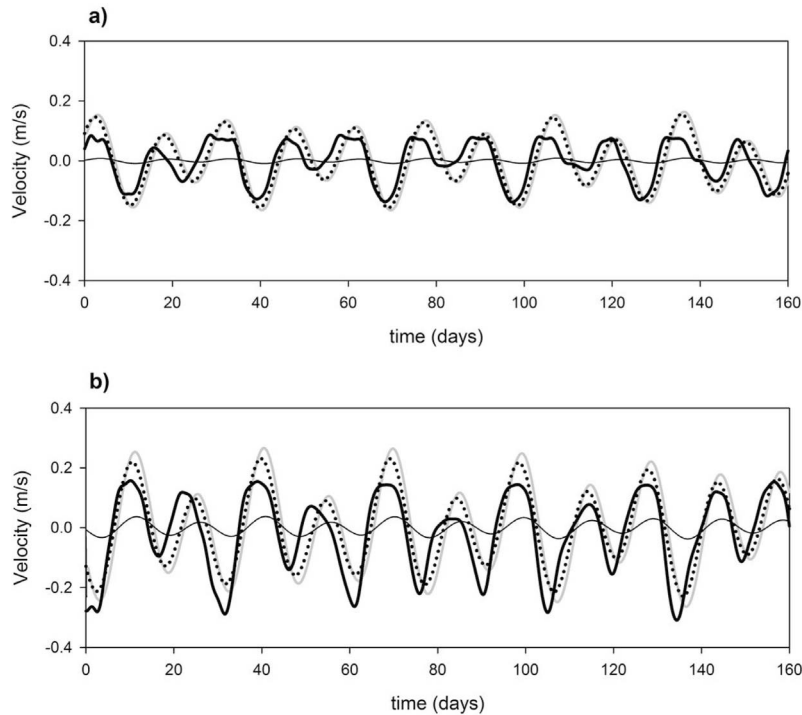
Figure 6. Time series of subinertial currents at Camarinal Sill cross section. Simulated by the numerical model with friction (thick black curve), first-order contribution considering all terms in equations (38) and (39) (gray curve), only considering the first term (dotted curve), and joined contribution of the last two terms (thin black curve): (a) upper layer and (b) lower layer. Series begin at 0000 UTC on 16 October 1995.

behavior of tidal subinertial oscillations in the current velocity. Accepting this result, the following simpler expression for first-order contribution to subinertial currents is proposed:

$$\in u_1^1 d_1 = \langle u_1^0 \xi_i^0 \rangle \qquad (43)$$

$$\in u_2^1 d_2 = -\langle u_2^0 \xi_i^0 \rangle. \qquad (44)$$

Therefore, those first-order contributions may be basically interpreted in the framework of the volume conservation equations. In that context, expressions (43) and (44) represent additional transports needed to correct the zero-order tidal transports for the changes in the layer thickness due to vertical displacements of the interface in response to the internal tide. It implies a subtraction or addition of transport from or to the zero-order transport in each layer.

[30] Taking into account the difference in Greenwich phase between the vertical displacement of the interface and the velocity reported by *Bray et al.* [1990] and *Bryden et al.* [1994], or using the values given by the model simulations (see Table 2), in the upper layer the behavior implied would be a subtraction of transport during ebb tide (flow toward the Mediterranean) and flood tide (flow toward the Atlantic). Following the same reasoning, in the lower layer, that term would imply the addition of transport during ebb and flood tides. Figure 7 shows the evolution of those transports during a transition from neap to spring tides. As can be

seen, the instantaneous transports $u_1^0 \xi_i^0 / -u_2^0 \xi_i^0$ are practically negative/positive all the time. Note also that the low-pass filtered transports $\langle u_1^0 \xi_i^0 \rangle$ and $\langle -u_2^0 \xi_i^0 \rangle$ increase with tidal amplitude from neap to spring tide.

[31] Apart from the creation of a quarter diurnal signal, because those added transports keep in each layer the same sign during flood and ebb tide, they will make a clear contribution to the currents averaged over the complete tidal cycle. The larger the tidal oscillations the larger the contribution. Therefore, those terms must show significant low-frequency variability, with maxima and minima coincident with spring/neap tides, or more generally, with maxima/minima oscillations of tidal current and vertical interface displacement over the Sill.

[32] As shown in Figure 7, induced first-order transports have a different sign for upper and lower layers. As a consequence, when the subinertial current in the upper layer is positive (toward the east) in the lower layer, it is negative (toward the west) and vice versa; this provides a physical explanation for the baroclinic character of the tidally generated subinertial currents.

[33] This baroclinic character is also the factor responsible for the observed temporal behavior of the vertical shear of the horizontal currents. During spring tides, the subtraction/addition of transport in the upper/lower layers implies the creation of a negative/positive current velocity (toward the west/east). This behavior reduces the mean current intensity in both layers, and therefore the vertical shear of horizontal
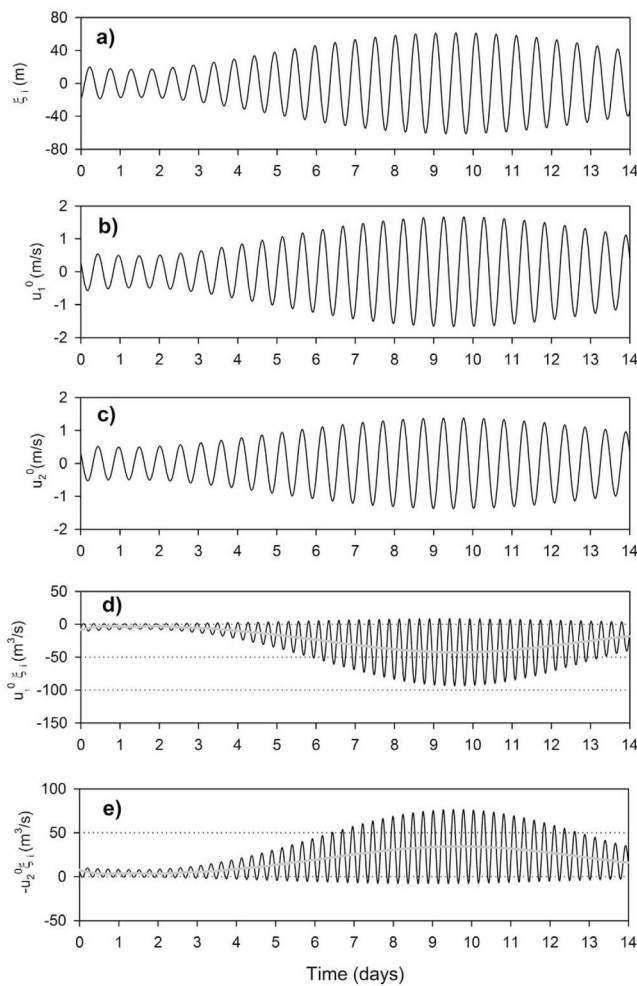
Figure 7. Temporal evolution of zero-order solutions built using the information of Table 2 and first-order transports as approximated by equations (43) and (44): (a) zero-order interface displacement, (b) zero-order upper layer velocity, (c) zero-order lower layer velocity, (d) instantaneous (black curve) and low-pass filtered (gray curve) transports for upper layer, and (e) instantaneous (black curve) and low-pass filtered (gray curve) transports for lower layer.

shear after removing the effect of the second EOF mode of subinertial currents and the vertical shear of the total signal. As can be seen, this mode exerts a clear control in defining the time behavior of vertical shear, and smoothes the variation in maximum values of vertical shear between spring and neap tide.

6. Conclusions

[35] As found in previous studies, the EOF analysis of records of subinertial currents on the Camarinal Sill yielded two dominant modes that together explain more than 90% of the total variance at all depths. The first (explaining about 85%/30% of variance in the upper/lower layers) presents a barotropic character and a rather irregular fluctuations; it is related basically to meteorological forcing. In contrast, the second mode (explaining about 15%/70% of variance in the upper/lower layer) is baroclinic and presents a clear deterministic behavior with time, which seems to be related to tidal forcing.

[36] Against the hypothesis put forward in previous studies, that tidal mixing cycles may explain the second EOF mode, we have used both numerical and analytical
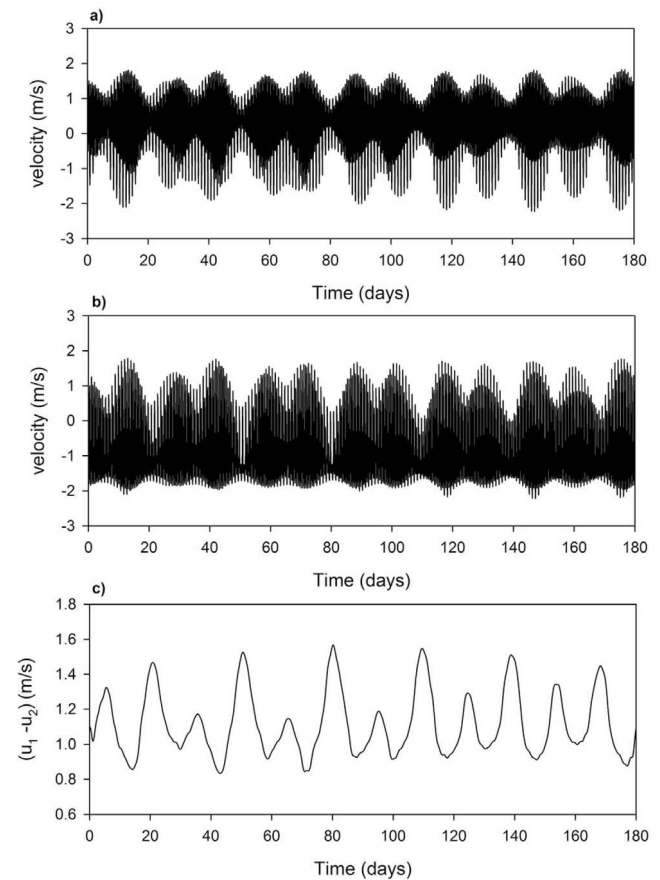
currents is also reduced. On the other hand, during neap tides the reverse situation is found. Now, a reduced transport is subtracted/added in the upper/lower layers, which leads to greater mean currents in both layers and an increased vertical shear, compared with during spring tides.

[34] Figures 8 and 9 show the vertical shear of the horizontal current deduced from the model and from the observations. As can be seen, in both the model and the observations, the shear reaches its maxima/minima values during neap/spring tides. The similarity between simulated and observed vertical shear indicates that the observed values are basically dominated by the deterministic mode of subinertial currents (second EOF mode of section 2). The importance of this mode in determining the temporal behavior of observed vertical shear is reinforced by the results shown in Figure 10, where we compare the vertical

Figure 8. Time series of velocity simulated with the numerical model at Camarinal Sill cross section: (a) total signal in the upper layer, (b) total signal in the lower layer, and (c) vertical shear of subinertial currents. Series begin at 0000 UTC on 16 October 1995.
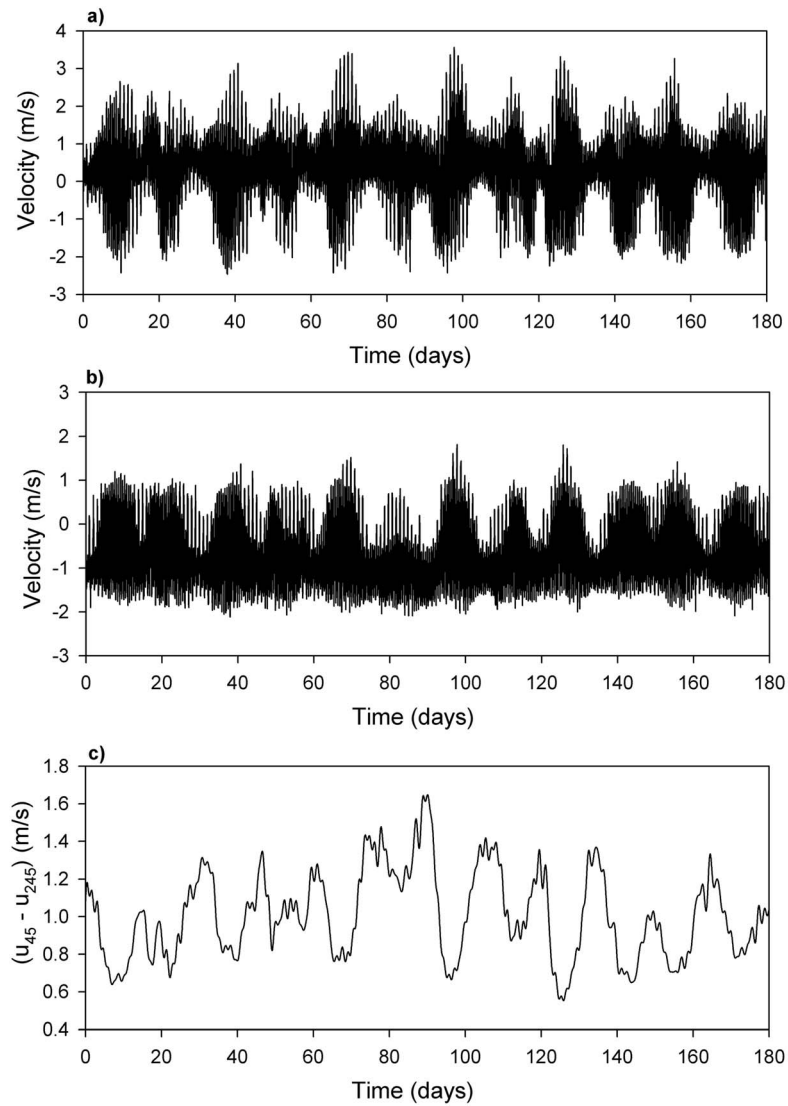
Figure 9. Same as Figure 7 except for recorded currents over Camarinal Sill. In Figure 9c the shear is represented by the difference of velocity between 45 and 255 m depth. Series begin at 1223 UTC on 16 October 1995.
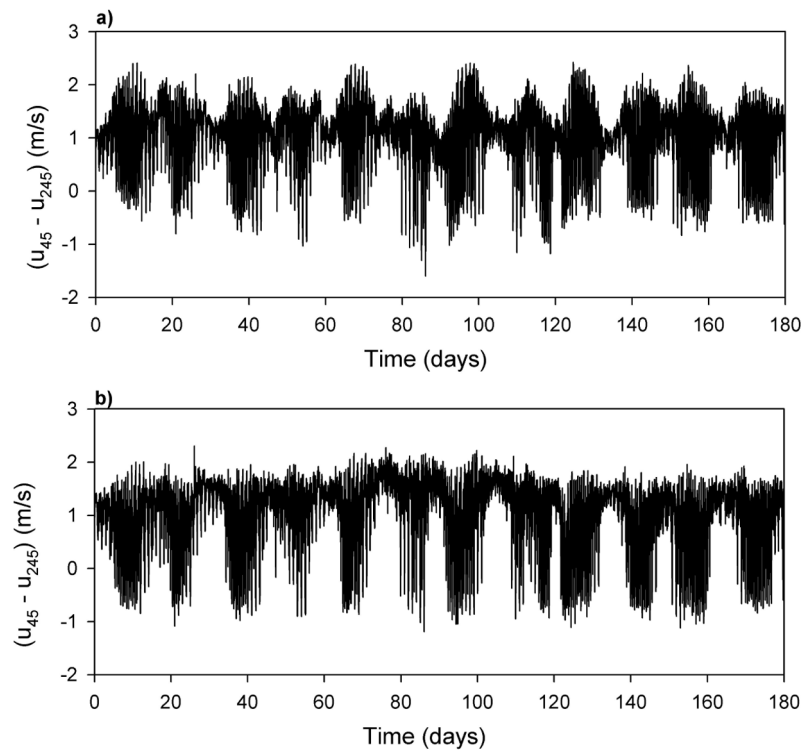
Figure 10. Vertical shear of recorded horizontal currents between depths of 45 and 255 m: (a) once contribution of the second EOF mode (deterministic mode) of the subinertial currents has been removed and (b) total signal. Time series begin at 1223 UTC on 16 October 1995.

procedures to show that this deterministic mode may be basically explained in terms of the nonlinear interactions among the main semidiurnal tidal constituents imposed by the volume conservation principle. We have also shown that the deterministic baroclinic mode is the main factor responsible for the vertical shear of subinertial currents that present their maximum/minimum values during neap/spring tides. More specifically, it minimizes the differences of maximum shear between neap and spring tides which could contribute to a more regular interfacial mixing intensity than would be expected if only semidiurnal tide dynamics are considered.

References

Brandt, P., A. Rubino, D. V. Sein, B. Baschek, A. Izquierdo, and J. O. Backhaus (2004), Sea level variations in the western Mediterranean studied by a numerical tidal model of the Strait of Gibraltar, *J. Phys. Oceanogr.*, *34*, 433–443, doi:10.1175/1520-0485(2004)034<0433:SLVITW>2.0.CO;2.

Bray, N. A., C. D. Winant, T. H. Kinder, and J. Candela (1990), Generation and kinematics of the internal tide in the Strait of Gibraltar, in *The Physical Oceanography of Sea Straits*, edited by L. J. Pratt, pp. 477–491, Kluwer Acad., Dordrecht, Netherlands.

Bryden, H., J. Candela, and T. H. Kinder (1994), Exchange through the Strait of Gibraltar, *Prog. Oceanogr.*, *33*, 201–248, doi:10.1016/0079-6611(94)90028-0.

Candela, J., C. Winant, and H. L. Bryden (1989), Meteorologically forced subinertial flows through the Strait of Gibraltar, *J. Geophys. Res.*, *94*, 12,667–12,679, doi:10.1029/JC094iC09p12667.

Castro, M. J., J. Macías, and C. Parés (2001), A *Q*-scheme for a class of systems of coupled conservation laws with source term. Application to a two-layer 1-D shallow water system, *Math. Model. and Numer. Anal.*, *35*(1), 107–127, doi:10.1051/m2an:2001108.

Castro, M. J., J. Macías, C. Parés, J. A. García-Rodríguez, and E. Vázquez-Cendón (2004a), A two-layer finite volume model for flows through channels with irregular geometry: Computations of maximal exchange solutions: Application to the Strait of Gibraltar, *Commun. Nonlinear Sci. Numer. Simul.*, *9*, 241–249, doi:10.1016/S1007-5704(03)00115-1.

Castro, M. J., J. A. García-Rodríguez, J. M. González-Vida, J. Macías, and C. Parés (2004b), Numerical simulation of two-layer shallow water flows through channels with irregular geometry, *J. Comput. Phys.*, *195*, 202–235, doi:10.1016/j.jcp.2003.08.035.

Farmer, D., and L. Armi (1986), Maximal two-layer exchange over a sill and through the combination of a sill and contraction with barotropic flow, *J. Fluid Mech.*, *164*, 53–76, doi:10.1017/S002211208600246X.

Foreman, M. G. G., and R. F. Henri (1989), The harmonic analysis of tidal model time series, *Adv. Water Resour.*, *12*, 109–120, doi:10.1016/0309-1708(89)90017-1.

García la Fuente, J., J. L. Almazán, F. Castillejo, A. Khribeche, and A. Hakimi (1990), Sea level in the Strait of Gibraltar: Tides sea level in the Strait of Gibraltar, *Int. Hydrogr. Rev.*, *LXVII*(1), 111–130.

Helfrich, K. L. (1995), Time-dependent two-layer hydraulic exchange flow, *J. Phys. Oceanogr.*, *25*, 359–373, doi:10.1175/1520-0485(1995)025<0359:TDTLHE>2.0.CO;2.

Izquierdo, A., L. Tejedor, D. V. Sein, J. O. Backhaus, P. Brandt, A. Rubino, and B. A. Kagan (2001), Control variability and internal bore evolution in the Strait of Gibraltar: A 2-D two-layer model study, *Estuarine Coastal Shelf Sci.*, *53*(5), 637–651, doi:10.1006/ecss.2000.0706.

Lacombe, H., and C. Richez (1982), The regime of the Strait of Gibraltar, in *Hydrodynamics of Semi-Enclosed Seas*, *Elsevier Oceanogr. Ser.*, vol. 34, edited by J. C. J. Nihoul, 13–73 pp., doi:10.1016/S0422-9894(08)71237-6, Elsevier, New York.

Tsimplis, M. S., and H. L. Bryden (2000), Estimation of the transports through the Strait of Gibraltar, *Deep Sea Res. Part I*, *47*, 2219–2242, doi:10.1016/S0967-0637(00)00024-8.

Vargas, J. M., J. García-Lafuente, J. Candela, and A. Sánchez Román (2006), Fortnightly and monthly variability of the exchange through the Strait of Gibraltar, *Prog. Oceanogr.*, *70*, 466–485, doi:10.1016/j.pocean.2006.07.001.

M. Bruno and A. Vázquez, Departamento de Física Aplicada, Universidad de Cádiz, Avda República Saharaui S/N, Puerto Real, E-11510 Cadiz, Spain. (miguel.bruno@uca.es)

J. M. González-Vida, Departamento de Matemática Aplicada, Universidad de Málaga, Campus de Teatinos, S/N, E-29081 Malaga, Spain.

J. Macías, Departamento de Análisis Matemático, Universidad de Málaga, Campus de Teatinos, S/N, E-29081 Malaga, Spain.